Lightweight, Proprioceptive, Origami-Inspired Soft Robotic Arm for High Payload, Low-Cost Reconfigurable Manipulation

Jiyang Wang[1], Yuchen You[1], Xinqi Zhang[1], Haobo Fang[1], Jiaqi Wang[2], Xiaonan Huang[2]

***Abstract*— Soft pneumatic robotic arms have emerged as promising alternatives to conventional rigid manipulators, offering compliance, adaptability, low-cost, and inherent safety for use alongside people. However, many existing designs suffer from limited workspace, low payload capacity, and poor resilience to external forces, restricting their applicability in industrial and field settings. In this work, we present a low-cost, lightweight, and modular soft robotic arm engineered for high payload capacity, precision control, and reconfigurability across diverse operational contexts. The arm is constructed from plug-and-play modules, each integrating three 3D-printed Yoshimura origami actuators for omnidirectional 3D bending, one 3D-printed Kresling origami structure with an embedded magnetic encoder for centerline length self-sensing, and one IMU for orientation measurement. This modular architecture enables on-the-fly customization of arm length, stiffness, and configuration, allowing for task-specific optimization without requiring significant hardware changes. The complete arm, composed of four such modules, achieves a reach of over 1100 mm, 10 mm position repeatability, over 10 kg payload capacity, and 3+ degrees of freedom, while maintaining a lightweight 3 kg structure with a total material cost under $2,000. Its soft, compliant structure reduces the risk of injury during accidental contact, making it well-suited for safe operation alongside people in dynamic environments. We validate the arm's performance through payload testing, precision assessment, and modular reconfiguration experiments, demonstrating its potential for use in long-duration warehouse automation, autonomous inspection, sample collection, and space exploration. These results indicate that the proposed arm design offers a scalable, cost-effective, and robust alternative to conventional rigid manipulators, with potential for wide-scale deployment in next-generation robotics.**

I. INTRODUCTION

Soft robotic arms are emerging as a compelling alternative to conventional rigid manipulators, offering intrinsic compliance, enhanced adaptability, low cost, and improved safety for operation alongside people in unstructured or dynamic environments. These features make them particularly well-suited for field-based, mobile, and space applications, where unpredictable contact and environmental variability are common. However, many existing soft robotic systems face significant challenges, including limited workspace, low payload capacity, poor robustness, no state estimation, and reliance on bulky support infrastructure. These limitations often stem from the use of complex fluidic networks, and soft materials with low mechanical strength as well as the lack of compact onboard sensing, which collectively hinder their scalability, precision, and practical deployment in real-world settings.

To overcome the limitations of existing soft robotic arms, we introduce a low-cost, lightweight, proprioceptive, and modular origami soft robotic arm engineered for high payload capacity, precision control, and reconfigurability. The arm is constructed from plug-and-play modules, each integrating three vacuum-driven 3D-printed Yoshimura origami actuators for omnidirectional 3D bending, one 3D-printed Kresling origami structure with an embedded magnetic encoder for centerline length self-sensing, and one IMU for orientation measurement. This modular architecture enables on-the-fly customization of arm length, stiffness, and configuration, allowing for task-specific adaptation without significant hardware changes. A fully assembled arm, composed of four such modules, achieves a reach of over 1100 mm, 10 mm position repeatability, omnidirectional 3D bending with over 10 kg payload capacity, and vertical lifting capability for loads over 20 kg, while maintaining a lightweight 3 kg structure with a total material cost under $2,000. Each module offers 3 degrees of freedom, providing a high level of dexterity and adaptability for a wide range of tasks.

Compared to rigid industrial arms such as the Fanuc CRX-20iA, which weighs approximately 40 kg with a maximum payload of 10 kg, our soft robotic arm achieves a much higher payload-to-mass ratio, supporting up to 10 kg payload with a total weight of only 3 kg. This design offers not only lightweight construction but also reliable and repeatable performance enabled by a hierarchical control framework. At the high level, a Piecewise Constant Curvature (PCC) geometric model combined with a damped least-squares optimization function is used to resolve redundancy and compute unique pose solutions in a kinematically redundant system. At the low level, a PID controller regulates actuator lengths to track the desired configuration accurately.

We validate the arm's performance through payload testing, precision assessment, and modular reconfiguration experiments, demonstrating its potential for use in long-duration warehouse automation, autonomous inspection, sample collection, and space exploration. These results indicate that the proposed arm design offers a scalable, cost-effective, and robust alternative to conventional rigid manipulators, with potential for wide-scale deployment in next-generation robotics.

[1] Jiyang Wang, Yuchen You, Xinqi Zhang, and Haobo Fang are with the EECS Department, University of Michigan, Ann Arbor, MI, USA
realwjy, yuchenxr, dadaaa, fanghb@umich.edu
[2] Jiaqi Wang and Xiaonan Huang are with the Robotics Department, University of Michigan, Ann Arbor, MI, USA
wangjq, xiaonanh@umich.edu

II. METHODOLOGY

A. Mechanical Design

Compared to conventional rigid robotic arms that rely on heavy metal components and high-torque motors, the proposed soft robotic arm achieves a dramatic reduction in weight—approximately 3kg for the full system, including sensing, actuation, and structure. This is nearly ten times lighter than traditional counterparts with similar reach and payload capacity (typically around 30kg). Such a reduction improves portability and energy efficiency while significantly enhancing safety, especially in mobile or human-collaborative environments.

Despite its lightweight construction, the arm supports payloads over 10kg during omnidirectional 3D bending tasks and over 20kg during vertical lifting, demonstrating a favorable payload-to-mass ratio under both dynamic and static loading conditions. These values highlight the arm's suitability for terrestrial industrial applications where flexibility, modularity, and adaptability are essential. Moreover, the system's payload capacity can be further improved by employing a more powerful vacuum pump or by scaling up the actuators. This scalability offers a tunable design space, enabling performance optimization for application-specific requirements without fundamentally altering the system architecture.

Each module features a compact, highly adaptable actuation unit constructed from three 3D-printed Yoshimura origami actuators arranged in a tripod configuration, which enables omnidirectional bending and axial contraction by independently controlling the vacuum pressure in each actuator. This layout allows a single module to occupy a spacious three-dimensional workspace, providing considerable dexterity within a small footprint. Compared to conventional linear actuators such as bellows, the Yoshimura-tripod structure offers significantly higher bending stiffness and better directional controllability, making it more suitable for high-payload manipulation tasks. Additionally, the origami geometry achieves a high contraction ratio of up to 3.5:1, enabling substantial length reduction and large-angle, full 3D motion within a compact form factor.

Central to each module is a 3D-printed Kresling origami structure that functions as a sensor for self-sensing centerline length by measuring the twisting angle. Its inherent geometric coupling between axial contraction and rotational twist enables real-time estimation of the centerline length with the aid of an encoder. Unlike conventional kinematic or dynamics-based estimation methods, this approach leverages the physical deformation behavior of the structure itself, improving model robustness across a wide range of payloads. A diametrically magnetized element embedded at the Kresling tip, in conjunction with a Hall-effect encoder recessed in the adjacent plate, provides a direct measurement of the twist, yielding accurate estimates of axial strain and external loading conditions. Notably, the Kresling unit operates as a passive element and does not reduce degrees of freedom, thereby preserving the mechanical simplicity and full actuation range of the surrounding Yoshimura actuators. This embedded sensing strategy enhances the system's compactness, precision, and repeatability.

To complement this sensing capability, each module also incorporates a BNO085 inertial measurement unit (IMU), which provides real-time orientation data for closed-loop control. These embedded sensors—duplicated in every module—enable full-body onboard state estimation.

Structurally, the origami actuators are mounted to carbon-fiber–reinforced PPA (PPA-CF) end plates that integrate air channels and mechanical fastening interfaces. The pneumatic pathways are embedded directly into the flange, connecting the actuators to external valves via air tubes. Modules are assembled using twelve symmetrically arranged captive M5 screws through pre-aligned flange holes, creating joints that resist torsional and bending loads and provide clamping forces exceeding 500N.

Each module occupies a bounding volume of approximately $255\,\mathrm{mm} \times 255\,\mathrm{mm} \times 225\,\mathrm{mm}$, forming a compact triangular prism. The Yoshimura origami actuators is designed to fit within a cylindrical envelope of $222\,\mathrm{mm}$ in length and $75\,\mathrm{mm}$ in diameter. The central Kresling origami sensor is composed of two stacked units, each confined within a cylindrical volume of $10.5\,\mathrm{mm}$ in height and $24\,\mathrm{mm}$ in diameter. The structural components are primarily fabricated using FDM 3D printing on a Bambu Lab platform. The end flanges and pneumatic routing structures are printed using PPA-CF. If needed, the PPA-CF parts can be substituted with other materials such as PLA-CF, PA6-CF, rigid 10k, carbon fiber or metal.

The three Yoshimura origami actuators within each module are printed using Bambu TPU 95HF. The central Kresling origami structure is printed using TPE 75A. All origami elements can also be fabricated via silicone molding as an alternative to 3D printing, or replaced with other soft materials like latex rubber which has comparable hardness and mechanical response.

Together, these design choices create a robust, lightweight, and intelligent actuation unit—highly suitable for dynamic, collaborative, and industrial environments requiring reconfigurable and soft robotic systems.

B. Electrical System

As shown in Fig. 2, the proposed control architecture adopts a hierarchical design that integrates high-level trajectory planning with low-level actuator control to enable coordinated motion in soft robotic systems. At the high level, a PC computes the target actuator lengths based on the desired trajectory and an optimization function. A Piecewise Constant Curvature (PCC) kinematic model is employed to estimate pose and perform inverse kinematics, ensuring accurate motion control via closed-loop control.

At the core of the low-level system (Fig. 3) lies the NUCLEO H755ZI-Q microcontroller, which orchestrates both sensing and actuation. It communicates bidirectionally with a custom-designed driver board that serves as a centralized interface, linking sensors and actuators across all modules.

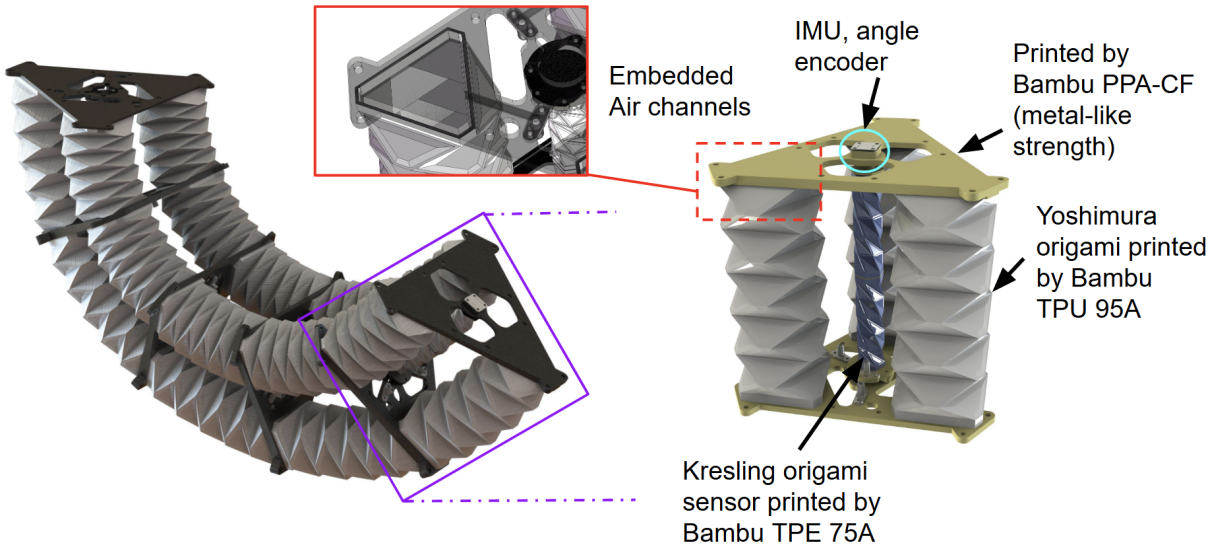

Fig. 1. Modular design featuring a quick-release mechanism for rapid assembly and disassembly, embedded pneumatic and electric routing reducing the number of external tubing or cabling, and parallel Yoshimura origami to enable multi-axis motion with enhanced structural stability and a compact form factor.

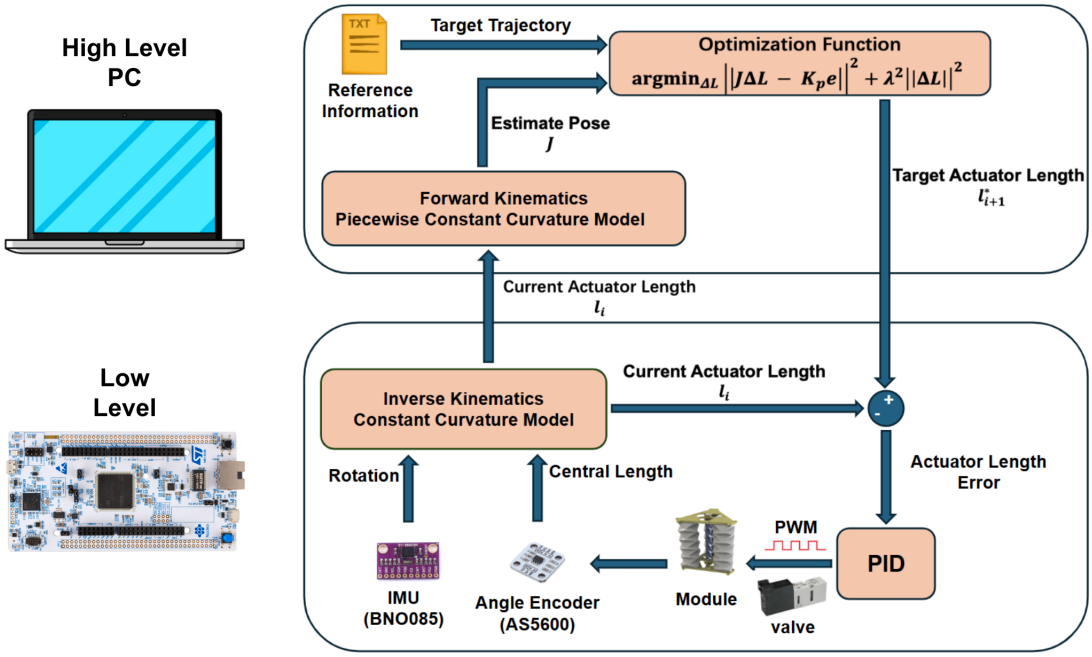

Fig. 2. Overview of the soft robotic arm's control architecture. A two-tier system integrates high-level motion planning and low-level hardware control. The PC computes target actuator lengths using a PCC model, while the STM32 microcontroller reads sensor data to estimate pose and regulates pneumatic valves with PID feedback for accurate actuation.

Each module is equipped with a dedicated sensor array comprising an Inertial Measurement Unit (BNO085) and a Hall-effect angle encoder (AS5600). The IMU captures the Euler angles of the module's base plane to estimate the end effector direction of the module, while the encoder measures the twisting angle of the central Kresling origami actuator to estimate the central length of the module. Leveraging the geometric relationship between twisting and length, the system infers the real-time centerline length between adjacent modules, enabling reconstruction of both axial extension and rotation.

As illustrated in Fig. 4, the custom-designed driver board consists of two main subsystems: communication ports and control ports.

On the communication side, an I2C multiplexer enables sequential access to multiple sensor modules with identical addresses, eliminating conflicts and supporting scalability. NMOS transistors are integrated to selectively power individual sensor channels, improving signal integrity and reducing

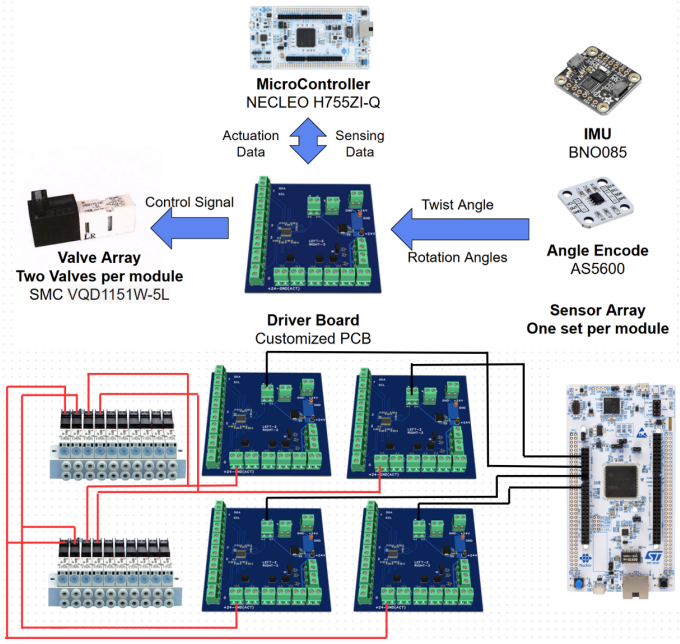

Fig. 3. Electrical architecture for low-level control of the soft robotic arm. A Nucleo microcontroller communicates with a custom PCB to coordinate sensing and actuation across modules. Each module includes an IMU and angle encoder for real-time configuration feedback. Valve arrays are actuated via digital and PWM signals to regulate cavity pressure and achieve precise deformation.In the image further down, the red lines represent I2C connections, and the black lines represent digital/PWM connections.

interference.

On the control side, the board provides dedicated ports for valve actuation. Digital signals are used for discrete source switching, while PWM signals allow proportional flow control. This dual-mode signaling supports both binary and analog pressure regulation across multiple modules.

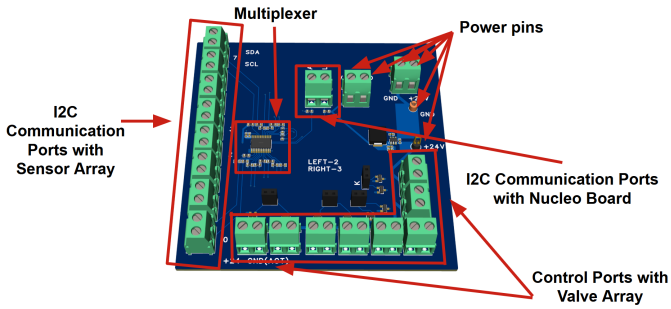

Fig. 4. Custom PCB driver board integrating I²C-based sensor communication and solenoid valve control. An onboard multiplexer manages address conflicts among sensor modules, while NMOS transistors control power to individual channels. Control ports deliver digital or PWM signals to valves, and dedicated power and I²C interfaces support scalable expansion.

Further details of the pneumatic regulation process are depicted in Fig. 5. Each valve module connects to a continuous vacuum supply via a vacuum pump and chamber. The three-way valve, driven by digital logic, selects the pressure source, while PWM modulates the two-way valve to control the actuation duration. This combination enables smooth and responsive control over actuator internal pressure and contraction.

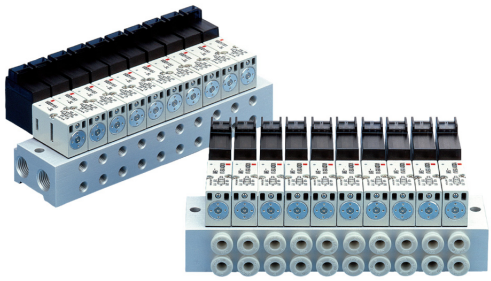

Fig. 5. Valve configuration for pressure control. Each module includes a three-way valve for source selection and a two-way valve for flow modulation. The array structure allows simultaneous control of multiple modules in the soft robotic arm.

As shown in Fig. 6, the full low-level control loop includes sensor feedback processed under the PCC assumption, where each module's peripheral chambers are assumed to share constant curvature. Based on real-time sensor readings, the system computes the lengths of three chambers and updates actuator targets. A PID controller minimizes the length error to ensure compliant, accurate deformation.

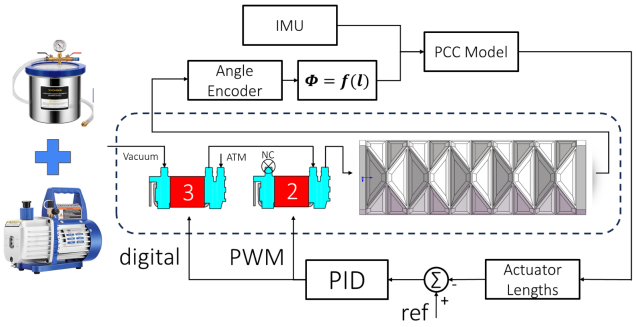

Fig. 6. Valve-based pressure regulation and sensing-feedback loop for soft actuator control. A digital signal selects between vacuum and atmospheric pressure via a three-way valve, while a PWM signal regulates flow through a two-way valve. Sensor data (IMU and angle encoder) feeds into a PCC model to estimate actuator length, which is corrected by a PID loop for precise deformation tracking.

In summary, the proposed system features a modular hardware-software architecture that tightly integrates sensing, control, and actuation. At the hardware level, a custom PCB interfaces with an STM32-based microcontroller to manage sensor communication and valve operation. Each module includes a sensor array and dual-valve unit for real-time estimation and precise pressure modulation. The software stack builds on PCC-based kinematics and PID feedback, enabling accurate and scalable control for soft robotic actuation.

C. Module's Kinematics Model

1) Spaces and Variables: Each module k ($k = 1, 2, \ldots, n$) is driven by three origami-inspired actuators. Denote by l_{kj}, $j = 1, 2, 3$, the current length of the j-th actuator in module k. We then define:

TABLE I

TERMINOLOGY, SUBSCRIPT k MEANS THE K-TH MODULE OF THE ARM

name	notes
Q_k	the configuration space with basis $\kappa_k, \phi_k, \beta_k$
κ_k	module curvature
ρ_k	radius of curvature
ϕ_k	rotation angle in the x-y plane
β_k	pitch angle
$\vec{q}_k$	the configuration space vector, $q_k = \begin{bmatrix}\kappa_k, \phi_k, \beta_k\end{bmatrix}^T$
$\dot{q}_k$	the configuration space vector differentiated by time, i.e. $\frac{d}{dt}\vec{q}_k$
X	the task space
$\vec{x}_k$	the task space vector
$\vec{l}_k$	the actuation space with basis l_{kj} for $j = 1, 2, 3$
$\dot{l}_k$	the actuation space vector differentated by time, i.e. $\frac{d}{dt}\vec{l}_k$
l_{kj}	the actuation vector of the k-th module's j-th origami
l_{C_k}	the central curve length of the module
J_{XQ}	the Jacobian matrix from configuration space (Q) to task space (X)
$\vec{v}$	translational velocity in the task space (X)
$\vec{\omega}$	angular velocity in the task space (X)
R_k^{k-1}	$\mathbb{R}^{3\times3}$ rotational matrix from the $k-1$-th module's end plane to the k-th module's end effector
P_k^{k-1}	$\mathbb{R}^3$ translational vector (displacement vector) from the $k-1$-th module's end plane to the k-th module's end effector
$\text{Rot}(Z, \phi_k)$	$\mathbb{R}^{3\times3}$ rotational matrix with respect to Z axis in the k-th module's local coordinate, and rotated angle ϕ_k
T_k^{k-1}	$\mathbb{R}^{4\times4}$ translation matrix which maps the current $k-1$-th module's input direction vector to the next module's direction vector with displacement and direction change
$\vec{e}$	error in the task space, namely the displacement from the arm's current position to its target position expressed by $\Delta x, \Delta y, \Delta z$

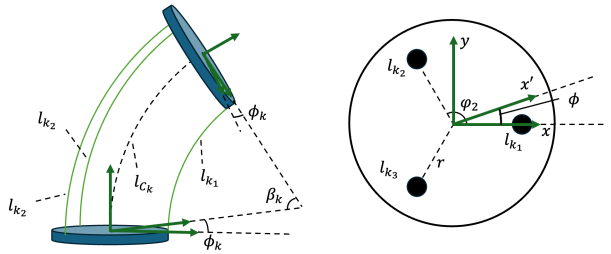

Fig. 7. The Piecewice Constant Curvature model of each module, which means that the 3 origami's curvature within each module has identical curvature κ, and the whole arm module will have a rotational angle ϕ and pitch angle β

- **Actuation space:**

$$\vec{l}_k = \begin{bmatrix} l_{k1} & l_{k2} & l_{k3} \end{bmatrix}^T \in \mathbb{R}^3.$$

- **Configuration space:**

$$\vec{q}_k = \begin{bmatrix} \kappa_k & \phi_k & \beta_k \end{bmatrix}^T \in \mathbb{R}^3,$$

where
  - κ_k is the constant curvature,
  - ϕ_k is the bending plane angle in the xy-plane,
  - β_k is the radius-of-curvature parameter.

- **Task space:** the end-point position of module k,

$$\vec{x}_k = \begin{bmatrix} x_k & y_k & z_k \end{bmatrix}^T \in \mathbb{R}^3.$$

All symbols are summarized in Table I.

2) Geometric Mapping: Under the Piecewise Constant Curvature (PCC) assumption, each module behaves like a circular arc. We first compute the mean segment length

$$l_{C_k} = \frac{1}{3}\sum_{j=1}^{3} l_{kj}.$$

Introduce the auxiliary angles, which are detailed demonstrated in the Fig. 7

$$\varphi_{kj} = \frac{2\pi}{3}(j-1), \quad j = 1, 2, 3, \quad \Delta_{kj} = r\cos\big(\varphi_{kj} - \phi_k\big),$$

where r is the nominal radius of the origami pattern. Then the inverse mapping $L_k \mapsto Q_k$ is given by

$$\beta_k = \frac{2}{3r}\sqrt{\sum_{j=1}^{3} l_{kj}^2 - \sum_{i<j} l_{ki}\, l_{kj}}, \tag{1}$$

$$\phi_k = \operatorname{atan2}\big(3(l_{k2} - l_{k3}),\ \sqrt{3}\,(l_{k2} + l_{k3} - 2l_{k1})\big), \tag{2}$$

$$l_{kj} = l_{C_k} - \beta_k \Delta_{kj}, \quad j = 1, 2, 3. \tag{3}$$

Together, these yield the full configuration vector q_k from the measured actuator lengths l_k.

3) Forward Kinematics: Section-to-Section Transform: Each module defines a local homogeneous transform

$$T_k^{k-1} = \begin{bmatrix} R_k^{k-1} & P_k^{k-1} \\ \mathbf{0}_{1\times3} & 1 \end{bmatrix},$$

where the rotation

$$R_k^{k-1} = \text{Rot}(Z,\, \phi_k)\ \text{Rot}(Y,\, \beta_k)\ \text{Rot}(Z,\, -\phi_k) \tag{4}$$

is the standard Z–Y–Z Euler sequence and the translation

$$P_k^{k-1} = \frac{1}{\rho_k}\begin{bmatrix}(1-\cos\beta_k)\cos\phi_k, & (1-\cos\beta_k)\sin\phi_k, & \sin\beta_k\end{bmatrix}^T. \tag{5}$$

Chaining n modules gives the end-effector pose

$$T_n^0 = T_1^0\, T_2^1\, \cdots\, T_n^{n-1}.$$

4) Jacobian and Velocity Mapping with Actuation Space: Denote by $\vec{q} = [q_1^T, \ldots, q_n^T]^T$ the stacked configuration vector and $\vec{l} = [l_1^T, \ldots, l_n^T]^T$ the stacked actuator lengths. The velocity relationship is

$$\dot{l} \;=\; J_{LQ_n}\,\dot{q},$$

where $\dot{l}, \dot{q}$ is the time differentiated form of the vectors $\vec{l}$ and $\vec{q}$, and $J_{LQ_n} \in \mathbb{R}^{3n\times3n}$ is block-lower-triangular:

$$J_{LQ_n} = \begin{bmatrix} J_{L_1Q_1} & 0_{3\times3} & \cdots & 0_{3\times3} \\ J_{L_1Q_1} & J_{L_2Q_2} & \ddots & \vdots \\ \vdots & \ddots & \ddots & 0_{3\times3} \\ J_{L_1Q_1} & \cdots & \cdots & J_{L_nQ_n} \end{bmatrix}.$$

Here each local Jacobian from the configuration space to the actuation space for the k-th module is:

$$J_{L_kQ_k} = \begin{bmatrix} 1 & r\beta_k\sin(\phi_k - \varphi_{k1}) & -r\cos(\varphi_{k1} - \phi_k) \\ 1 & r\beta_k\sin(\phi_k - \varphi_{k2}) & -r\cos(\varphi_{k2} - \phi_k) \\ 1 & r\beta_k\sin(\phi_k - \varphi_{k3}) & -r\cos(\varphi_{k3} - \phi_k) \end{bmatrix}$$

5) Linear and Angular Velocity Computation: Under the Piecewise Constant Curvature (PCC) assumption, a small change in the configuration coordinate $\dot{q} \in \mathbb{R}^{3k}$ produces both a linear velocity $v_{\text{end}} \in \mathbb{R}^3$ and an angular velocity $\omega_{\text{end}} \in \mathbb{R}^3$ of the end-effector. These are related by the task-space Jacobian $J_{XQ} \in \mathbb{R}^{6\times 3k}$:

$$\begin{bmatrix} v_{\text{end}} \\ \omega_{\text{end}} \end{bmatrix} = J_{XQ}\,\dot{q} = \begin{bmatrix} J_{vQ} \\ J_{\omega Q} \end{bmatrix} \dot{q}.$$

a) Linear Velocity: The $3 \times 3k$ block J_{vQ} is obtained by combining different blocks of local Jacobians $J_{v_k Q_k}$. And the local Jacobians are calculated by differentiating the end-point position (x, y, z) with respect to each configuration basis (κ, ϕ, β), where the task space coordinate could be expressed by (5). In each module it has the form

$$J_{v_k Q_k} = \begin{bmatrix} \frac{\partial x}{\partial \kappa_k} & \frac{\partial x}{\partial \phi_k} & \frac{\partial x}{\partial \beta_k} \\ \frac{\partial y}{\partial \kappa_k} & \frac{\partial y}{\partial \phi_k} & \frac{\partial y}{\partial \beta_k} \\ \frac{\partial z}{\partial \kappa_k} & \frac{\partial z}{\partial \phi_k} & \frac{\partial z}{\partial \beta_k} \end{bmatrix} \tag{6}$$

And to stack up the modules to calculate the velocity of the end effector, according to equation of Changing Coordinate, it states like following:

$$\vec{v}_{\text{end}} = \vec{v}_{\text{prev}} + {}^{\mathcal{B}_{\text{final}}}\dot{\vec{p}}_{\text{final/prev\_base}} + \vec{\omega} \times \vec{p}_{\text{final/prev\_base}} \tag{7}$$

and then to express in the linear form for the first k modules' cumulated translational Jacobian $J_{v_k,Q_k} \in \mathbb{R}^{3\times 3k}$:

$$J_{v_k,Q_k} = \begin{bmatrix} \left(J_{v_{k-1},Q_{k-1}} - \left(R_k^0 P_k^{k-1}\right)^{\wedge} J_{\omega_{k-1},Q_{k-1}}\right)^T \\ \left(R_k^0 J^l_{v_k,Q_k}\right)^T \end{bmatrix}^T \tag{8}$$

b) Angular Velocity: Similarly, $J_{\omega Q}$ is the $3\times 3k$ block that maps length rates to end-effector angular velocity by combining each local angular Jacobians $J_{\omega_k Q_k}$. The local angular Jacobian can be obtained by the equation

$$\vec{\omega} = (\frac{d}{dt}R)R^T \tag{9}$$

where R is the rotation matrix mentioned in the equation (4). And now $\vec{\omega}$ is a function in the basis of configuration space (κ, ϕ, β), which could be used to do differentiation with respect to q_k basis.

And to stack up the modules to calculate the angular velocity of the end effector, according to equation of Changing Coordinate, it states like following:

$$\vec{\omega}_{\text{end}} = \vec{\omega}_{\text{prev}} + \vec{\omega}_{\text{final/prev\_base}} \tag{10}$$

and then to express in the linear form for the first k modules' cumulated angular Jacobian $J_{\omega_k,Q_k} \in \mathbb{R}^{3\times 3k}$:

$$J_{\omega_k,Q_k} = \begin{bmatrix} J_{\omega_{(k-1)}Q_{(k-1)}} & R_{k-1}^0 J_{\omega_k Q_k} \end{bmatrix} \tag{11}$$

Thus, stacking all k modules yields the full Jacobian J which simultaneously computes both the linear and angular velocity of the soft arm's end-effector.

6) Task-Space Jacobian: Finally, from Eq. (8) and Eq. (11) splitting position and orientation,

$$\dot{x}_{\text{end}} = \begin{bmatrix} J_{vQ} \\ J_{\omega Q} \end{bmatrix} \dot{q} = \underbrace{\begin{bmatrix} J_{vQ} \\ J_{\omega Q} \end{bmatrix} \times J^{-1}_{LQ_n}}_{J_{XL}} \dot{l},$$

we obtain the full mapping $J_{XL} : \mathbb{R}^{3n} \to \mathbb{R}^6$ from actuator-space velocities to end-effector twist.

7) Control Unit: Since the control system will focus only on a microscopic view of the change in actuator length in each loop, namely Δl_{kj} within very short time interval. And thus actually the control algorithm needs to calculate the length change rate $\dot{l}$ for each actuator. The control target $\vec{x} = (x, y, z)$ is in the target space world coordinate, that's where Jacobian J_{XL} become fairly helpful, that

$$\begin{bmatrix} \Delta x & \Delta y & \Delta z \end{bmatrix}^T = J_{XL}\Delta\vec{l} \tag{12}$$

which can also expressed similarly in the change of error vector $\Delta\vec{e}_{control} = J_{XL}\Delta\vec{l}$.

Intuitively, the control target is to minimize the end error, when given the current error e_p. Namely the purpose could be expressed formally as

$$\min ||\vec{e}_p - \Delta\vec{e}_{control}|| \tag{13}$$

8) Redundancy Resolution: Because J_{XL} is generally tall ($6\times 3n$ with $n > 2$), we resolve redundancy via damped least squares:

$$\Delta\vec{l}^* = \arg\min_{\Delta\vec{l}} \left\| J_{XL}\,\Delta\vec{l} - k_p\,\vec{e}_p \right\|^2 + \lambda^2 \|\Delta\vec{l}\|^2,$$

where $\vec{e}_p$ is the desired task-space error, k_p is a unitless proportional gain and $\lambda > 0$ also a unitless regularization term. This yields a stable, unique solution for $\Delta\vec{l}$ in each control cycle.

III. Results

To validate the robustness and scalability of the proposed modular system, we conducted a set of experiments focused on payload capacity, structural resilience, and operational repeatability, as shown in Fig. 8.

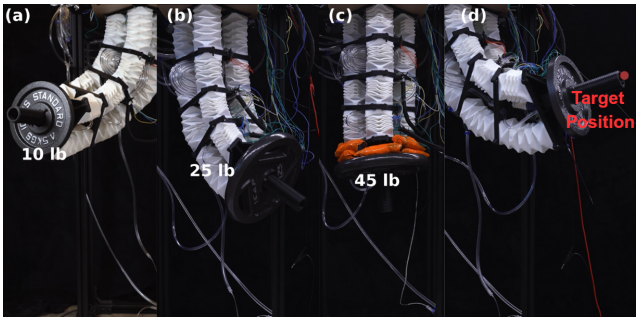

Fig. 8. Figures showing (a) the soft arm lifting a 10 lb payload, (b) the soft arm lifting a 25 lb payload, and (c) the soft arm lifting a 45 lb payload. (d) verifies the repeatability of the arm's performance under repeated actuation.

A. Payload Test

The soft robotic arm, assembled in its dual-module configuration, was tasked with lifting progressively heavier loads of 10 lb (4.5 kg), 25 lb (11.3 kg), and 45 lb (20.4 kg), significantly exceeding the actuator's own weight. These trials demonstrate not only the high payload-to-weight ratio of the system, but also its structural integrity under demanding load conditions.

The ability to lift a 45 lb payload vertically, as shown in Fig. 8(c), represents a payload-to-mass ratio exceeding 7:1, highlighting the exceptional force amplification enabled by the embedded pneumatic actuation and the structurally efficient origami architecture. In addition, the system maintained stable behavior and showed no signs of structural failure or control degradation throughout all trials, underscoring its resilience and suitability for high-force tasks.

B. Repeatability Test

In addition to payload capacity, we evaluated the system's repeatability by subjecting it to repeated actuation cycles while tracking end-effector positioning (Fig. 8(d)). The arm consistently returned to the target position within a positional tolerance of ±10 mm, confirming reliable performance over time. This level of repeatability, achieved with minimal sensor drift or mechanical fatigue, affirms the viability of the arm for tasks requiring high consistency in both terrestrial and space-based applications.

In general, these results demonstrate the soft arm's mechanical robustness, reliable control performance, and scalable architecture capable of adapting to varying task demands through rapid module addition or replacement. Such versatility is essential for autonomous operations in complex and resource-constrained space environments, where adaptability and resilience are critical for long-term deployment.

IV. Conclusion

In this work, we developed a low-cost, lightweight, and modular soft robotic arm that overcomes key limitations of existing soft manipulators, including limited payload capacity, restricted workspace, lack of state estimation, and poor resilience. By integrating 3D-printed Yoshimura and Kresling origami structures with embedded sensing and a hierarchical control framework, the arm achieves high payload-to-mass ratio, precision, and task-specific reconfigurability. Experimental results validate its scalability, robustness, and suitability for dynamic, real-world environments such as warehouse automation. The proposed design demonstrates a promising, scalable alternative to traditional rigid manipulators for next-generation robotic applications.